



HAL
open science

Multibeam Laser Plasma Interaction at Gekko XII laser facility in conditions relevant for Direct-Drive Inertial Confinement Fusion

Gabriele Cristoforetti, P. Koester, S. Atzeni, D. Batani, S. Fujioka, Y. Hironaka, Stefan Hüller, T. Idesaka, K. Katagiri, K. Kawasaki, et al.

► **To cite this version:**

Gabriele Cristoforetti, P. Koester, S. Atzeni, D. Batani, S. Fujioka, et al.. Multibeam Laser Plasma Interaction at Gekko XII laser facility in conditions relevant for Direct-Drive Inertial Confinement Fusion. High Power Laser Science and Engineering, 2023, 11, pp.1-11. 10.1017/hpl.2023.13 . hal-03997437

HAL Id: hal-03997437

<https://cnrs.hal.science/hal-03997437>

Submitted on 20 Feb 2023

HAL is a multi-disciplinary open access archive for the deposit and dissemination of scientific research documents, whether they are published or not. The documents may come from teaching and research institutions in France or abroad, or from public or private research centers.

L'archive ouverte pluridisciplinaire **HAL**, est destinée au dépôt et à la diffusion de documents scientifiques de niveau recherche, publiés ou non, émanant des établissements d'enseignement et de recherche français ou étrangers, des laboratoires publics ou privés.

Multibeam Laser Plasma Interaction at Gekko XII laser facility in conditions relevant for Direct-Drive Inertial Confinement Fusion

G. Cristoforetti,^{1,*} P. Koester,¹ S. Atzeni,² D. Batani,³ S. Fujioka,⁴ Y. Hironaka,⁴ S. Hüller,⁵ T. Idesaka,⁴ K. Katagiri,⁶ K. Kawasaki,⁴ R. Kodama,⁴ D. Mancelli,⁷ Ph. Nicolai,³ N. Ozaki,^{4,6} A. Schiavi,² K. Shigemori,⁴ R. Takizawa,⁴ T. Tamagawa,⁴ D. Tanaka,⁴ A. Tentori,³ Y. Umeda,^{6,8} A. Yogo,⁴ and L.A. Gizzi¹

¹*Intense Laser Irradiation Laboratory, INO-CNR, Pisa, Italy*

²*Dipartimento SBAI, Università di Roma 'La Sapienza', Roma, Italy*

³*Université Bordeaux, CNRS, CEA, CELIA, Talence, France*

⁴*Institute of Laser Engineering, Osaka University, Osaka, Japan*

⁵*Centre de Physique Théorique CPHT, CNRS, IP Paris, Ecole Polytechnique, Palaiseau, France*

⁶*Graduate School of Engineering, Osaka University, Osaka, Japan*

⁷*Institute of Plasma Physics and Lasers, Hellenic Mediterranean University Research Centre, Rethymnon, Greece*

⁸*Institute for Integrated Radiation and Nuclear Science, Kyoto University, Sennan, Osaka, Japan*

(Dated: January 19, 2023)

Laser Plasma Interaction and hot electrons have been characterized in detail in laser irradiation conditions relevant for direct-drive Inertial Confinement Fusion. The experiment has been carried out at Gekko XII laser facility in multibeam planar geometry at intensity $\sim 3 \cdot 10^{15}$ W/cm². Experimental data suggest that high-energy electrons, with temperature 20-50 keV and conversion efficiencies $\eta < 1\%$, were mainly produced by the damping of electron plasma waves driven by Two Plasmon Decay. Stimulated Raman Scattering is observed in a near-threshold growth regime, producing a reflectivity of $\sim 0.01\%$, and is well described by an analytical model accounting for the convective growth in independent speckles. The experiment reveals that both TPD and SRS are collectively driven by multiple beams resulting in a more vigorous growth than that driven by single-beam laser intensity.

INTRODUCTION

In Direct-Drive Inertial Confinement Fusion (ICF)[1, 2] a millimeter-sized spherical capsule containing a cryogenic mixture of Deuterium and Tritium is irradiated by multiple laser beams, that ablate the external plastic shell, driving the compression and the heating of the fuel up to its ignition. The efficiency of the compression can be however reduced by the onset of laser-plasma instabilities, as Stimulated Brillouin Scattering (SBS) [3, 4] and Cross-Beam Energy Transfer (CBET) [5], that can produce a loss of laser energy and an unbalance of laser beam coupling. Moreover, compression can be deteriorated by suprathermal hot electrons (HE) with energy $\gtrsim 50$ keV, generated during laser-plasma interaction, that can be absorbed by the cold fuel, enhancing its entropy and preventing ignition. It was estimated that a tolerable level of HE energy coupled to the cold fuel, i.e. not so large to prevent the fuel ignition, is of the order of 0.15% of the laser energy[6]. During laser-plasma interaction at typical ICF intensities ($I = 10^{14} - 10^{15}$ W/cm²), HE are mainly produced via wave-particle interaction in electron plasma waves (EPW), which are in turn produced by the onset of parametric instabilities, as Stimulated Raman Scattering (SRS) [3, 4], and/or Two Plasmon Decay (TPD) [7]. A correct understanding of the parameters affecting the SRS/TPD growth and their ability to generate HE in conditions of interest for Direct-Drive ICF is therefore needed for mitigating their effect on fuel ignition.

Many experiments were carried out at the OMEGA laser facility[8–11] on this issue, both in planar and spherical irradiation geometry, producing an extensive knowledge of laser-plasma interaction (LPI) at laser intensity $I = 10^{14} - 10^{15}$ W/cm². Experiments identified the TPD as the main source of HE and showed that it is driven collectively by multiple beams, scaling with the parameter $I_{ov}L/T$, where I_{ov} is the intensity associated with overlapping laser beams, $|L = n/(dn/dx)|$ is the electron density scalelength and T is the electron temperature, all the values calculated at the quarter critical density $n_c/4$ for the laser light ($n_c \approx 1.1 \cdot 10^{21} \lambda^{-2}$ cm⁻³ and λ_0 is the laser wavelength expressed in μm). In addition to the $I_{ov}L/T$ parameter, the threshold of TPD also depends on the geometry and polarization of the laser beams, determining the efficiency of their coupling, which results in the generation of commonly driven EPWs[12]. Experiments reported HE temperatures in the range of 20-90 keV[8–10], increasing with $I_{ov}L/T$, and maximum conversion efficiencies of laser energy to HE of $\sim 1\%$. The investigation of LPI at full-scale Direct-Drive ICF conditions at OMEGA laser is however made complex by laser energy limitations. Long plasmas expected in the full-scale scenario ($L \approx 600 \mu\text{m}$) could be here obtained only by using ad hoc target geometries; such experiments, where shallow-cone targets were used, suggested that convective SRS tends to become dominant over TPD in plasmas with a longer density scalelengths and irradiated at a higher laser intensity [13].

LPI studies in conditions relevant for direct-drive ig-

This peer-reviewed article has been accepted for publication but not yet copyedited or typeset, and so may be subject to change during the production process. The article is considered published and may be cited using its DOI.

This is an Open Access article, distributed under the terms of the Creative Commons Attribution licence (<https://creativecommons.org/licenses/by/4.0/>), which permits unrestricted re-use, distribution, and reproduction in any medium, provided the original work is properly cited.

10.1017/hpl.2023.13

nition ($L \approx 600 \mu\text{m}$, $T > 3 \text{ keV}$, $I \sim 10^{15} \text{ W/cm}^2$) were also recently carried out at the National Ignition Facility (NIF), where laser beams were arranged to be focused in planar geometry [14, 15]. Results showed a LPI regime significantly different from that obtained at OMEGA with spherical and planar targets and in agreement with shots made with shallow-cone targets, with HE mainly driven by SRS rather than by TPD. Moreover, the HE conversion efficiency was much higher than that measured at OMEGA, reaching up to 5% of laser energy; according to recent measurements [16], a fraction of them, consisting of $\sim 0.2 - 0.4\%$ of laser energy, is able to couple with and preheat the unablated shell, an amount which is therefore slightly above the dangerous limit of 0.15%. These results suggest that a more extensive knowledge on the transition between TPD-dominated and SRS-dominated regimes, on the parameters affecting SRS threshold/growth and on the scaling of HE, are needed, in order to mitigate their effects.

In the present work we report results of an experiment, carried out at the GEKKO XII laser facility in planar multi-beam irradiation geometry, able to explore the transition region between TPD- and SRS-dominated regimes, where both parametric instabilities and HE generation are characterized in detail. In agreement with the framework depicted by previous experiments, the results here show that TPD is driven in a saturated regime while SRS steeply grows in near threshold conditions with modest values of light reflectivity $\sim 10^{-4}$. This situation suggests a preponderant role of TPD in the generation of hot electrons, through the damping of the daughter plasma waves, as also indicated by the scaling of their temperature with the parameter $I_{ov}L/T$. The experimental data also suggest that both SRS and TPD are collectively driven by multiple beams, scaling with the intensity of the overlapped beams rather than with the single beam intensity. It is finally shown that for obtaining a correct modeling of SRS reflectivity in such experimental conditions it is crucial to take into account both the overlapping of the laser beams as well as the distribution of local values of laser intensities into the beam speckles.

EXPERIMENTAL SET-UP

The laser beam arrangement and the setup of diagnostics available at the GEKKO XII laser facility is sketched in Fig.1(a). The facility, located at the Institute of Laser Energy (ILE) of Osaka University, consists of 12 beams, bundled in an overall $f/3$ focusing cone entering the vacuum chamber through the same 12-inches port. Each beam, with Gaussian time profile, is focused at normal incidence on the planar target by a $f/15$ lens. In the present experiment, three laser beams ($\lambda_{driver} = 527 \text{ nm}$, $\tau = 230 \text{ ps}$, $E_{tot} = 270 \text{ J}$), hereafter *driver* beams,

were frequency doubled and used to generate a tenuous preplasma, while the remaining nine beams ($\lambda_0 = 351 \text{ nm}$, $\tau = 230 \text{ ps}$, $E_{each} = 80 \text{ J}$), hereafter *interaction* beams, were delayed by 200 ps and used for LPI investigation. The driver beams were smoothed by using kinoform phase plates (KPP) and were focussed to a flat top focal spot of $\sim 850 \mu\text{m}$ diameter in order to create an approximately 1D expanding plasma; the overlapped driver peak intensity $I_{ov}^{driver} \approx 1.8 \cdot 10^{14} \text{ W/cm}^2$ was sufficiently low to avoid the onset of parametric instabilities. The interaction beams were smoothed by random phase plates (RPP) and focussed to an overall approximately Gaussian spot of $\sim 280 \mu\text{m}$ FWHM, while the Gaussian spot of the single beams had $\sim 140 \mu\text{m}$ FWHM; the average bundle and the single beam peak intensities were therefore in the range $\langle I_{ov} \rangle = (2.2 - 3.4) \cdot 10^{15} \text{ W/cm}^2$ and $I_{SB} = (1.2 - 1.8) \cdot 10^{15} \text{ W/cm}^2$, respectively, depending on the shot statistics. Since the spatial distribution of the different beams into the focal spot is not uniform, regions with higher values of overlapped intensity I_{ov} could be present. These circumstances can play a role in the onset of collective LPI processes.

The focal spot size of driver and interaction beams could be inferred by an X-ray pinhole camera, acquiring an X-ray image of the plasma with a $15 \mu\text{m}$ aluminum filter at a spatial resolution of $30 \mu\text{m}$. As visible in Fig.2(a), the profiles obtained in both the irradiation configurations show in fact an inner peak with FWHM of $\sim 280 \mu\text{m}$ due to the interaction beams, while the profile obtained in the shots with the driver beams shows a larger base with FWHM $\sim 850 \mu\text{m}$.

Targets consisted of thin multilayer flat foils, as shown in Fig.1(b), including (i) a 10-50 μm -thick polystyrene ablation layer, (ii) a 5 μm -thick Copper layer, used as a tracer of HE via K_α line emission, and in a few shots (iii) a 20 μm -thick polyethylene back layer, aimed at reducing the effect of HE refluxing on the Cu K_α emission. Different values of the ablator layer thickness were here used with the aim of estimating the temperature of HE through the consequent variation of the Cu K_α emission.

The experiment made use of several diagnostics, which are described in detail in a separate publication [17]. Here, we describe only the subset of diagnostics which are devoted to characterize the LPI, the generation of hot electrons and their propagation into the target.

The backscattered light, showing signatures of SRS and TPD, was collected behind the last turning mirrors of two different interaction laser beams, namely beams #1 and #3 in Fig.1(c). After a suitable filtering, the signals were spectrally characterized in the UV-Vis range by using a time-integrated spectrometer (Ocean Optics, HR2000) and a time-resolved spectrometer, consisting of a spectrograph coupled to an optical streak camera (Hamamatsu, C7700). Sweep times of 1.6 ns and 5.2 ns were used in the streak camera acquisitions, resulting in time resolution of 20 ps and 50 ps, respectively. Light

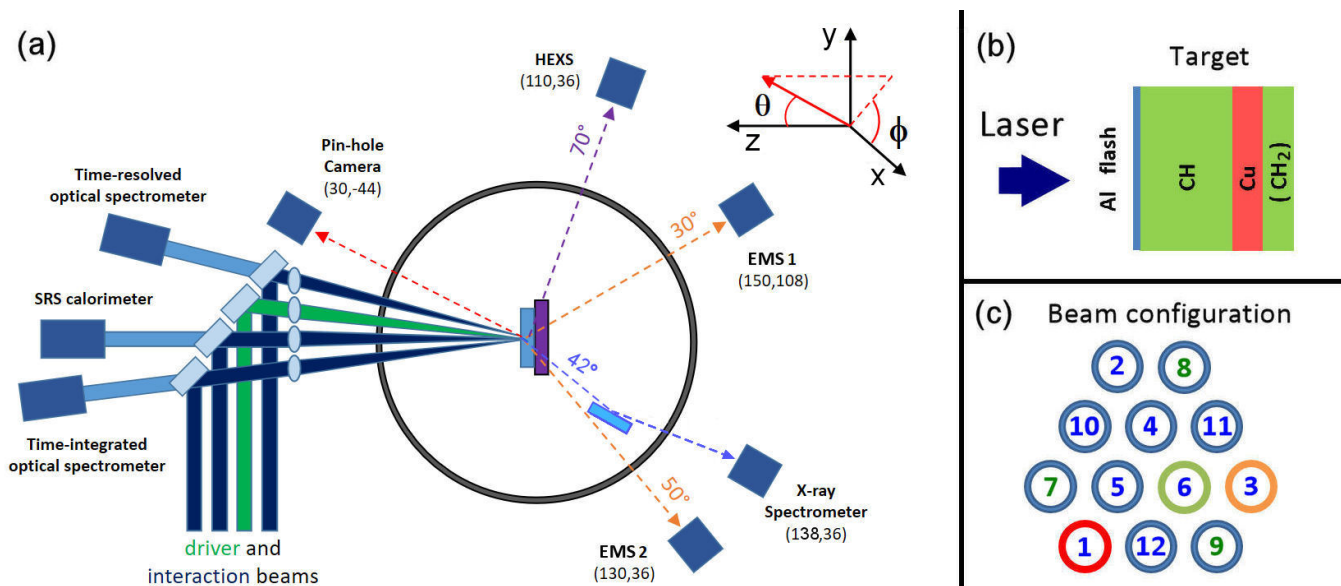


FIG. 1. a) scheme of the experimental setup. For the sake of simplicity, here the diagnostics are plotted in a plane, conserving the angles from the normal direction to the target. In the real setup, diagnostics are arranged at ports located in a spherical chamber. Below each diagnostics, polar (θ) and azimuthal (ϕ) angles of the corresponding port are reported. b) Target multilayer structure, consisting of an Al flash coating, a Polystyrene layer (CH), a Cu tracer layer and a Polyethylene layer (CH₂), starting from the laser irradiation side. c) laser beam configuration in the bundle. Green and Blue numbers refer to driver and interaction beams, respectively. Behind the turning mirrors in Ports 1, 3 and 6 the time-integrated optical spectrometer, the optical streak camera and the SRS calorimeter are located, respectively.

was conveyed to the time-resolved spectrometer through a 20 m quartz fiber, which made necessary a spectral-dependent temporal correction of the measured spectrum due to the light dispersion inside the fiber.

The amount of light backscattered by SRS in the laser focussing cone was measured by a calorimeter located behind the last mirror of an interaction laser beam, namely beam #6 in Fig.1(c). The light was filtered by suitable longpass, shortpass and notch filters with the aim of reducing as much as possible the contribution of residual laser and harmonics light. Due to the small amount of SRS in the present shots, a careful cross-calibration of calorimeter and time-integrated spectral measurements was also needed to quantify the amount of spurious light contribution in the measured values. Finally, the time-integrated SRS reflectivity was calculated after a correction for the spectral transmissivity of the optical line, which was determined by means of dedicated measurements.

Energy and amount of HE were investigated by using a Cu K α spectrometer, two electron magnetic spectrometers and a Bremsstrahlung cannon. K α fluorescence emission of Copper ($\lambda = 1.5406 \text{ \AA}$) is produced by the $2p \rightarrow 1s$ transition of an inner electron of a copper atom into a vacancy created by a collision of a hot electron with a K-shell electron. X-ray spectra with 0.05 keV energy resolution in the energy range 7.4-8.4 keV, including the Cu K α line (8.048 keV), were obtained by spectrally

dispersing the X-rays with an HOPG (Highly Ordered Pyrolytic Graphite) crystal and recording the signal with Imaging Plates (IP)[18]. The crystal was located on the rear side of the target at 42° from the normal to the target surface (polar angle $\theta = 132^\circ$, azimuthal angle $\phi = 36^\circ$) sending the signal on the X-ray spectrometer ($\theta = 138^\circ$, $\phi = 36^\circ$).

The Bremsstrahlung cannon, named High-Energy X-ray Spectrometer (HEXS) at GEKKO XII facility, was located behind the target at 70° from the normal ($\theta = 110^\circ$, $\phi = 36^\circ$). It measured the X-ray spectrum by using a stack of imaging plate layers separated by filters consisting of foils of increasing Z materials, from Al to Pb. The X-ray spectrum was here mainly produced by the Bremsstrahlung emission of HE propagating into the target, and could therefore be utilized to obtain the temperature of the hot electrons via comparison with dedicated GEANT4 simulations [19].

Finally, two Electron Magnetic Spectrometers (EMS), were located inside the interaction chamber, looking at the target from the rear side at 30° and 50° from its normal direction (EMS 1, $\theta = 150^\circ$, $\phi = 108^\circ$; EMS 2, $\theta = 130^\circ$, $\phi = 36^\circ$). They allowed the electron energy spectrum to be obtained in the range from 0.06 MeV to 1 MeV, through the energy spatial dispersion induced by magnets of 28 mT over imaging plate detectors.

Fujifilm BAS-MS imaging plates were used for EMS, HEXS and Cu K α diagnostics; they were scanned by us-

ing a Typhoon FLA 7000 scanner at a delay from the exposure time going from 30 to 50 minutes depending on the diagnostics.

INTERACTION CONDITIONS

The processes at play in laser plasma interaction depend on local conditions of interaction, as local values of laser intensity, electron temperature, plasma expansion velocity, electron density, as well as their spatial gradients. These conditions are here modelled by 2D radiative-hydrodynamic simulations carried out with the DUED code[20] for both the shots with and without the driver beams. The values of plasma temperature and density scalelengths, calculated at densities in the range 0.1-0.25 n_c , are reported in Fig.2(b) for different times. Hydrodynamic simulations show that plasma conditions are dominated by the interaction beams, with coronal temperatures in the underdense plasma in excess of 2 keV in proximity of the laser peak in both the irradiation configurations. The density scalelength of the plasma increases with time, with values of $\sim 80 \mu\text{m}$ and $\sim 120 \mu\text{m}$ at the laser peak time and after 200 ps respectively, in case of interaction beam only; the use of the driver beams leads to a modest rise of these value of $\sim 15\%$ ($L \sim 100 \mu\text{m}$ at laser peak and $L \sim 150 \mu\text{m}$ after 200 ps), which however is enough to modify significantly the growth of SRS as shown below.

Local conditions of interaction are here also determined by the partial overlap of the single beam focal spots on the target surface. As discussed in literature and observed in previous experiments, this condition can drive collective SRS and TPD[21], where common daughter waves are driven by different beams. This leads to a decrease of the threshold of the instabilities, as discussed below.

Finally, local conditions of interaction are here modified by the formation of laser speckles, produced by the Random Phase Plate. Here, the spatial manipulation of the laser coherence operated by the RPP splits a single beam into ~ 2000 speckles of size $l_{\perp} = 1.2\lambda_0 f_{\#} = 6.3 \mu\text{m}$, where $f_{\#} = 15$ is the f-number of the single focusing lens. Assuming an exponential distribution of local laser intensity $f(I) \propto \exp(-I/I_0)/I_0$ into the speckles[22], it turns out that local intensities up to 7-8 times the envelope laser intensity I_0 are reached into the beam. Furthermore, the spatial modulation of local intensity favours the onset of ponderomotive self focussing of the speckles. Considering that the critical power for such instability at densities of 0.1 n_c and for a plasma temperature of 1.5 – 2 keV is $\sim 450 - 600$ MW, filamentation is expected to be driven already in speckles with intensity $I = I_0$, corresponding to a power of ~ 600 MW. This produces a further enhancement of the local laser intensity and modifies the density profile, potentially affecting

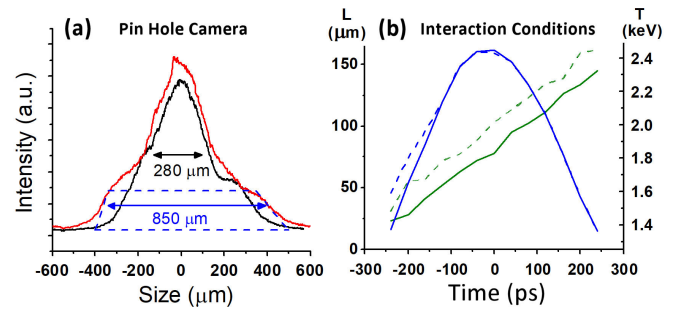


FIG. 2. a) Pinhole Camera profiles of laser spot obtained in shots with (red line) and without (black line) the driver beams. b) values of density scalelength L at the quarter of the critical density (green lines) and electron temperature (blue lines) obtained with DUED hydrocode[20]. Time on the x-axis refers to the peak of the interaction pulses. Solid and dashed lines represent conditions obtained without and with the use of the driver beams, respectively.

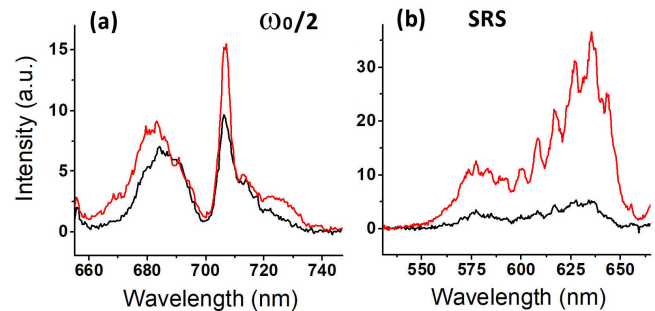


FIG. 3. Comparison of time integrated backscattered light spectra measured in shots with (red lines) and without (black lines) the driver beams. (a) $\omega_0/2$ emission peaks and (b) SRS spectra.

the growth of SRS on a longer scale[23].

EXPERIMENTAL RESULTS

Two Plasmon Decay

The onset of Two Plasmon Decay is usually investigated by the observation of the half-integer harmonics of laser light in the plasma emission spectrum [24], which are produced by the non linear coupling of plasma waves driven by TPD with laser light. Here, both time-resolved and time-integrated spectra showed evidence of half-harmonic $\omega_0/2$ of the interaction beam light ($\omega_0 = 2\pi c/\lambda_0$). The comparison of $\omega_0/2$ intensity obtained by switching on/off the beams into the bundle shows that half-harmonic light is emitted in a large cone, as expected, and only a small contribution ($\sim 20\%$) is scattered in the back direction.

Typical $\omega_0/2$ time-integrated spectra are reported in Fig.3(a), showing that the use of the driver beams re-

sults in a slight enhancement of the intensity, by a factor 1.2-1.3. As observed in previous works[24, 25], the spectrum exhibits three different features, all associated to instabilities driven in the proximity of the $n_c/4$ region. The origin of the different peaks, briefly reported in the following, has been discussed in Ref.25 and references therein, where the reader can find more details.

The narrowest red-shifted peak at $\lambda \sim 707$ nm is usually associated to a hybrid absolute TPD/SRS instability rather than to a pure absolute SRS, as reported by Seka et al.[24] and formalized by Afeyan and Williams[26]. This is the case limit of TPD driving a daughter electrostatic wave with $k \approx k_0$, which beats with the laser pump and generates an e.m. SRS-type backscattering wave. Since the frequency shift is here only produced by the plasma temperature according to the relation $\delta\omega/\omega_0 = 2.2 \cdot 10^{-3} T_{keV}$, this peak can be used as an accurate diagnostics of coronal temperature in the $n_c/4$ region[24]. Here, this approach provides a value $T \approx 1.8$ keV for all the shots, which is not far from that obtained by hydrodynamic simulations ($T_{hydro} = 2 - 2.4$ keV), considering the temporal integration of the spectral measurement.

Two other features are visible in the spectra, a large blue-shifted peak at $\sim 680-688$ nm and a symmetrical less intense red-shifted peak at $\sim 720-723$ nm, which are signatures of convective Two Plasmon Decay driven at densities lower than $n_c/4$. These peaks could be produced by Inverse Resonance Absorption of the EPWs near their turning point or by Thomson Downscattering of a laser photon coupling with the EPWs [27, 28]. Assuming that TPD grows on the maximum growth rate hyperbola, the wide spectra and the frequency shifts of these peaks indicate that TPD extends at densities significantly lower than $n_c/4$, resulting in perpendicular mode numbers k_{\perp} in the range $(0.2 - 2.9)\omega_0/c$. The blue peak observed in the shots with only the interaction beams at 686 nm, i.e. $\Delta\omega/\omega_0 \approx 1.1 \cdot 10^{-2}$, corresponds to EPWs driven at $n = 0.216 n_c$ with $k_e\lambda_D = 0.264$. When the driver beams are also used, both the blue and red peaks move to larger frequency shifts ($\Delta\omega/\omega_0 \approx 1.4 \cdot 10^{-2}$), denoting that TPD is pushed to lower densities, with maximum growth at $n = 0.204 n_c$ ($k_e\lambda_D = 0.31$). As already observed in similar experiments[25, 28], TPD is therefore spatially limited by the Landau damping of the EPWs and even extends to regions where the damping is strong. The spectra also suggest that EPWs propagate at angles of $\sim 40^\circ$ with respect to the pumping laser beam, and at slightly larger angles in shots with driver beams, which is expected to affect the divergence of HE accelerated into the EPWs.

Stimulated Raman Scattering

Time-integrated SRS spectra obtained in shots with and without the driver beams, measured by the time-integrated spectrometer, are reported in Fig.3(b). They show a broadband emission in the range 560 – 650 nm, with peaks at ~ 580 nm and ~ 630 nm; considering a coronal temperature of ~ 2.0 keV, Bohm-Gross dispersion relation indicates that SRS is driven in the region of densities from $0.11 n_c$ to $0.20 n_c$ and that the lower density region is limited by Landau damping of the EPWs ($k_e\lambda_D \approx 0.27$). Differently from the case of $\omega_0/2$ emission, the use of the driver beams results in a dramatic boost of SRS emission, by a factor of ~ 4 and ~ 6 in ports #6 and #1, respectively, where the SRS calorimeter and the time-integrated spectrometer were located. Despite the enhancement, calorimetric measurements show that SRS remains low, also in shots with the driver beams. The time-integrated SRS reflectivity, obtained by a cross correlation between calorimeter and spectrometer data, in fact, rises from $\sim 0.03\%$ in shots without driver beams to $\sim 0.09 - 0.16\%$ in shots with the preformed plasma.

SRS and TPD timing

The timing of TPD and SRS could be measured by time-resolved backscattered spectra acquired by the streak camera in port #3. Here, the presence of a spectral peak at $\lambda \approx 527$ nm could be observed only in shots where the driver beams were used, indicating that this feature was a signature of the the driver beams rather than a laser harmonic produced during the interaction. This allowed to use this feature as a fiducial for the absolute time calibration. A typical time-resolved spectrum in the spectral range 550-750 nm is shown in Fig.4 where the spectral signatures of the different instabilities have been highlighted by colored dashed lines. Frame (a) reports the time-integrated spectrum obtained by a vertical binning of the streaked spectrum on the streak camera, resembling the red curves shown in Fig.3 obtained with the UV-Vis spectrometer. As visible in frames (b) and (c), the absolute TPD/SRS and the convective TPD instabilities growing in proximity of the $n_c/4$ region are driven before the main laser peak, with a maximum extent at ~ 60 ps before the laser maximum. Differently, the convective SRS reaches its maximum extent in proximity of the laser peak. For a more clear evaluation of the timing of the various instabilities the time profile of driver and interaction beams are also reported in frame (d). The slight delay between TPD and convective SRS can be explained by the higher threshold of convective SRS with respect to that of TPD, so that higher values of laser intensity and density scalelength are needed for SRS growth. A similar result was previously found in Ref.[29], even if obtained in conditions of interaction

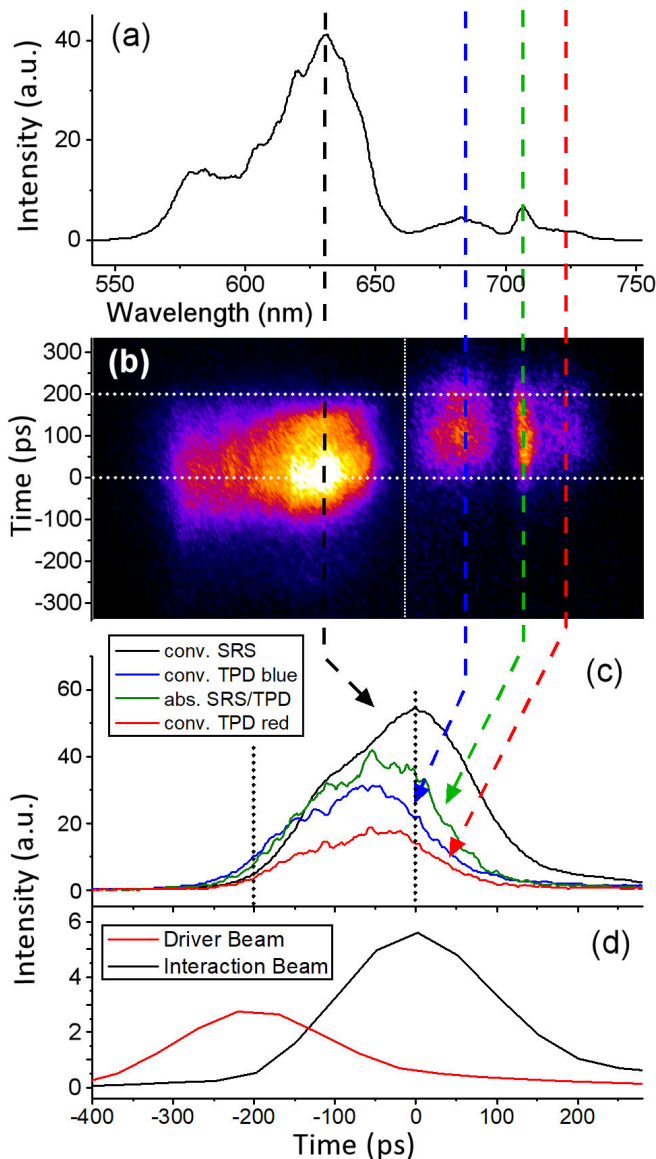


FIG. 4. Time-resolved spectra obtained for a shot where driver beams were used. (a) Time-integrated spectrum, obtained by vertical binning of the streaked spectrum shown in frame (b). (c) Time profile of the various spectral components observed in the spectrum. (d) Time profile of driver and interaction beam. The white and black dotted lines, in frames (b) and (c) respectively, indicate the times of driver and interaction beam peaks.

significantly different.

Multibeam LPI

In a few shots, some beams (#1, #5, #6 and #12) were switched off; the analysis of these shots can therefore provide information about the onset of collective multi-beam processes on LPI. In the shots where beam #1 was switched off, the SRS signal measured by the UV-

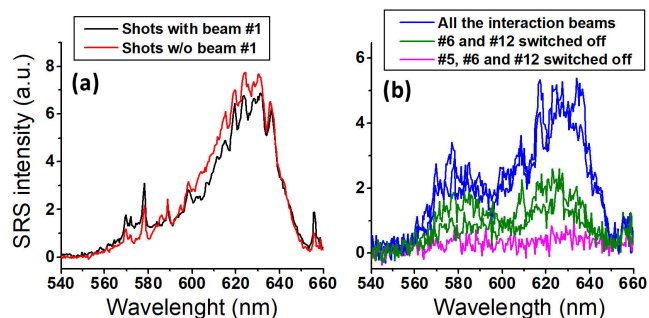


FIG. 5. Comparison of SRS spectra obtained in shots with a variable number of interaction beams. No driver beams were used in these shots. Time integrated spectrometer was located behind port #1. (a) Shots with (black line) and without (red line) the beam #1. (b) Shots with all the beams (blue lines) compared with shots where beams #6 and #12 (green lines) and #5, #6 and #12 (magenta line) were switched off.

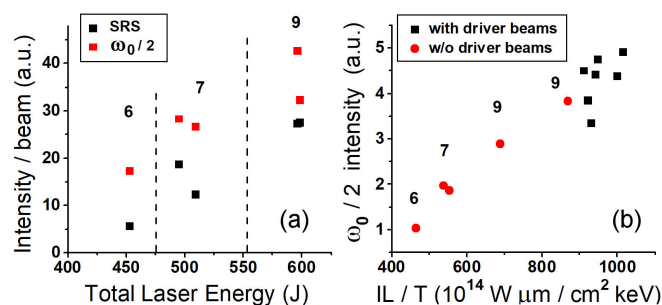


FIG. 6. (a) SRS and $\omega_0/2$ intensities normalized by the number of beams vs. the total laser energy. Measurements here refer to shots without the driver beams. Labels 6, 7 and 9 indicate the number of laser beams switched on in the shots. (b) growth of $\omega_0/2$ intensity versus the parameter $I_{ov}L/T$.

Vis spectrometer beyond port #1 remained substantially at the same level (Fig.5(a)); at the opposite, as shown in Fig.5(b), the SRS signal measured by the spectrometer was significantly reduced, down to 15% when the beams adjacent to port #1 were switched off. These results suggest that SRS light was not produced by purely backward SRS, but was significantly affected by the adjacent beams. A similar conclusion could be derived by switching off the beams in and around port #6, where the calorimeter was located.

Additional information are provided by the time-integrated intensities of SRS and $\omega_0/2$ features in the collected spectra, obtained by using only the interaction beams, plotted in Fig.6(a); here, signal intensities were normalized by the number of beams used. The graph shows that both SRS and $\omega_0/2$ intensities scale with the total laser intensity, rather than with the single beam intensity. This indicates that both SRS and TPD are driven by the collective action of different laser beams in some regions of the focal spot where more laser beams are overlapped; here, laser intensity is locally higher, re-

sulting in a boost of both parametric instabilities.

This result is strengthened by the scaling of $\omega_0/2$ signal intensity with the parameter $I_{ov}L/T$, which is shown in Fig.6(b), where all the shots with and w/o the driver beams are plotted; the parameter was here calculated by considering the overlapped laser intensity at the quarter critical density and plasma conditions at the time of TPD peak, as suggested by Fig.4. A similar scaling was already found in OMEGA experiments, where collective effects were clearly observed[8].

In collective processes, parametric instabilities driven by different laser beams share a daughter wave; considering the processes with the lowest thresholds[21, 30], it is expected that TPD and SRS here share a scattered EPW and e.m. wave, respectively. This hypothesis could explain why SRS light is not scattered in the back direction.

Hot Electrons

The energy of the HE propagating into the target was estimated by different diagnostics and compared. The spectra measured by the two EMS extended up to energies in excess of 400 keV, showing an exponential decay for energies higher than $\sim 150-180$ keV; the temperature of HE was therefore calculated by fitting the curve with a function $\propto \exp(-E/T_{hot})$ in the range 180-420 keV, as shown in Fig.7(a). Electrons with such energies are expected to be negligibly affected by the stopping power of the target and/or by the sheath field at the rear side of the target. Temperature values in the range from 20 to 50 keV were obtained by both EMSs, with slightly larger values for the EMS at a smaller angle (i.e. 30°). Following [8], in Fig.7(b) we plotted the HE temperatures obtained for all the shots, with and without the driver beams, versus the parameter $I_{ov}L/T$. As in Fig.6(b), the parameter was calculated by considering laser intensity at the quarter critical density and plasma conditions at the time of TPD peak; this is justified by the assumption, discussed below, that HE were here mainly accelerated by the TPD EPWs. As shown by the linear fit of the EMS data (indicated by the black and red dashed lines in the figure), both the spectrometers show a slight increasing trend of T_{hot} versus the $I_{ov}L/T$ parameter. HE temperatures obtained for the shots with the driver beams are usually larger than those obtained with only the interaction beams, which is explained by a higher value of $I_{ov}L/T$.

Bremsstrahlung Cannon measurements showed a detectable signal up to the 6-7 IP layers, depending on the shot. The detailed procedure followed to analyse the data is described in Ref.[31]; in short, it was performed in two steps by means of GEANT4 simulations. In a first stage, photons incident on the BSC were assumed to have an energy distribution given by $\propto \exp(-E/T_{ph})$ in order to fit the signal on each IP by a suitable photon tem-

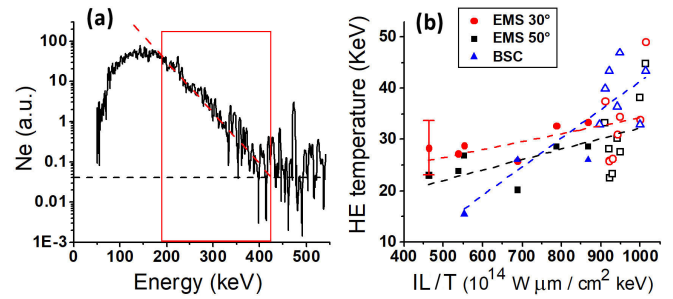


FIG. 7. (a) Typical HE spectrum obtained by Electron Magnetic Spectrometers, where the red rectangle shows the fitting region and the black dashed line is the background level. (b) Values of HE temperature obtained by the EMSs at 50° (black squares) and at 30° (red circles) and by the BSC (blue triangles) vs. the $I_{ov}L/T$ parameter. Solid and empty symbols indicate the shots without and with the driver beams. The relative uncertainty is 20% for all the datasets, indicated as an example by the error bar on the left. The dashed lines represent the linear fitting for the complete sets of EMS at 30° , EMS at 50° and BSC data.

perature T_{ph} (Fig.8(a)). In the second stage, electron bunches with energy distribution $\propto \exp(-E/T_{hot})$ were injected into multilayer targets used in the different shots in order to reproduce the photon distribution obtained in the first stage. For all the shots, this procedure resulted in HE temperatures $T_{hot} > T_{ph}$, which is produced by the energy-dependent scattering of electrons into the target. The temperatures obtained by the BSC analysis are in the range 15-50 keV and are overplotted in Fig.7(b). Considering the uncertainties of the EMS and the BSC data, with errors of $\sim 20\%$, the HE temperatures retrieved from all the diagnostics are quite close, despite the rising trend of BSC data with the $I_{ov}L/T$ parameter (blue dashed line) is a bit steeper. The reason of the different slope is not clear and could be produced by several factors, including the uncertainty of BSC analysis due to the two-step procedure and the angular selection of the HE population that is measured by the EMS, which can be non representative of the whole HE bunch and can depend on laser intensity.

The conversion efficiency of laser energy to hot electrons estimated by the BSC analysis was in the range $\eta = (0.4 - 0.6)\%$ for both the shots with and without the driver beams, showing no clear trend with laser intensity or $I_{ov}L/T$ parameter.

A confirmation of the T_{hot} values was finally obtained by reproducing with the GEANT4 simulations the K_α signal measured by using targets of different plastic thickness. Even if the GEANT4 code does not account for the hydrodynamic evolution and for the ionization state of the targets, its predictions are adequate for first-order interpretation of the experimental results[32, 33]. As shown in Fig.8(b), where only the data obtained by shots with the driver beams are shown, the K_α measured sig-

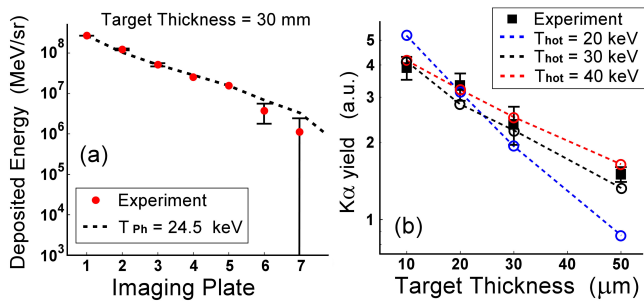


FIG. 8. (a) signal obtained in different IP in the BSC and calculated deposited energy calculated by GEANT4 simulations by using an exponential function with photon temperature of 24.5 keV. (b) $K\alpha$ intensity measured by using targets with different plastic thickness and calculated values by using $T_{hot} = 20, 30$ and 40 keV.

nal is well reproduced for T_{hot} between 30 and 40 keV, which is in agreement with the data shown in Fig.7(b).

DISCUSSION

It was previously shown that TPD scales with the parameter $I_{ov}L/T$ [8]. Here, the dependence of TPD on the parameter $I_{ov}L/T$ can be observed in Fig.6(b), where the $\omega_0/2$ intensities from both the shots with and w/o the driver beams are plotted together. An extensive study of LPI in similar conditions of interaction was previously done at OMEGA laser facility; in those experiments, TPD was found to rapidly grow for $I_{ov}L/T$ values going from the TPD threshold[34, 35], around $I_{ov}L/T \approx 230 \cdot 10^{14} \text{ W } \mu\text{m}/\text{cm}^2 \text{ keV}$, up to $I_{ov}L/T \approx (350 - 400) \cdot 10^{14} \text{ W } \mu\text{m}/\text{cm}^2 \text{ keV}$ [8]. In this range, the increase of TPD was associated to a rise of HE by two orders of magnitude. For higher values of $I_{ov}L/T$, TPD and HE increase more gently in an almost saturated stage. Here, laser intensity reaches values slightly higher than those explored at OMEGA laser[8, 9], implying slightly higher values of $I_{ov}L/T$ during TPD growth. Considering the range of $I_{ov}L/T$, going from 450 to $1000 \cdot 10^{14} \text{ W } \mu\text{m}/\text{cm}^2 \text{ keV}$, and the slope of the data in Fig.6 (comparable to that shown in Fig.4 of Ref.[8]), we can infer that TPD is driven in the saturation regime, well beyond the linear growth regime. The strong saturation of TPD is also suggested by the convective modes growing in low density regions, with perpendicular wavenumbers k_{\perp} reaching values close to $3 \omega_0/c$; these values are well beyond those observed at OMEGA laser and modelled by Yan et al.[36]. The growth in saturated regime explains why TPD is here only mildly affected by the use of the driver beams, as shown in Fig.3(a).

At times before the laser peak, TPD begins to damp and finally turns off. Possible mechanisms could be the steepening of the density profile at the quarter criti-

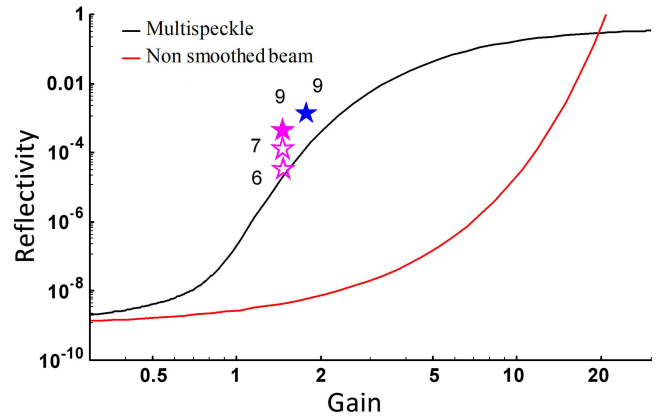


FIG. 9. Curves of growth of SRS reflectivity obtained from a multispeckle model (black) and a non smoothed beam (red) as a function of the Rosenbluth gain calculated for the nominal laser intensity. Magenta and blue stars represent experimental results in shots without and with the driver beams, respectively, where the gain has been calculated considering the single-beam intensity. Empty stars represent shots with a lower number of beams, as indicated by numbers 6,7,9. The relative uncertainty of the reflectivity values due to the calibration procedure is around 30%, which is as large as the star size.

cal density or the ion fluctuations produced by ponderomotive effects[37], as shown by Particle In Cell simulations[36].

SRS reaches its maximum growth after the peak of TPD, where the delay between the two instabilities is due to the higher threshold of SRS, which therefore needs higher values of laser intensity and density scalelength to be driven. Calorimetric measurements in shots without the driver beams show a very low value of SRS reflectivity of $(0.3 - 3) \cdot 10^{-4}$, with SRS features barely observed in the backscattered spectrum. The use of driver beams produces a boost of SRS, with an enhancement by a factor $\sim 4 - 6$, measured both by the calorimeter and by the spectrometer counts. According to hydrodynamic simulations, however, the interaction conditions of the main beams in the two cases are very similar, where a slight increase of density scalelength of only 10–20% is present in case of preplasma formation. No other relevant change in the interaction is expected.

In Fig.9, the measured values of SRS reflectivity (marked as stars) are compared with the classical model of convective gain in a linear density profile (red curve), given by Rosenbluth[38], where $R_{SRS} \approx 10^{-9} \exp(g)$. Here, the noise level was taken as $I_{noise} = 10^{-9} I_0$ [39], I_0 is the single beam laser intensity and the convective gain was calculated by $g = 2\pi\gamma_0^2/k'|\nu_e\nu_s|$, where γ_0 is the homogeneous growth rate, k' is the spatial derivative of the wavenumber mismatch of the interacting waves, and ν_e, ν_s are the group velocities of the plasma wave and of the scattering light wave. The SRS gains in Fig.9 are

calculated by considering single-beam laser intensity I_0 , whereas the effect of overlapping beams will be discussed later. It is evident that the experimental data would be reproduced by an amplification gain $g \sim 12$, which is expected for laser intensities in excess of 10^{16} W/cm², i.e. one order of magnitude higher than in our experiment. This discrepancy can be strongly reduced by taking into account the distribution of local laser intensity in the beam speckles, expected to reach up to 7-8 times the nominal single-beam laser intensity I_0 in the most intense ones. In a recent paper we presented a simple analytical model [23], able to reproduce the SRS reflectivity from a RPP smoothed laser beam, where the intensity of SRS scattered light is computed in each speckle via the classical Rosenbluth gain and the local intensities are distributed along the speckles according to a decreasing exponential function $f(I) = (1/I_0) \exp(-I/I_0)$. The model also accounts for the saturation of SRS in the most intense speckles, usually produced by pump depletion or by non linear effects, levelling their reflectivity to a constant value R_{sat} , which is obtained by experiments in the range $R_{sat} \sim 0.3 - 0.5$. As shown in Fig.9, the multispeckle model (black curve) almost reproduces the experimental data, suggesting that in the present interaction conditions the reflectivity is dominated by the onset of SRS in the most intense speckles[40]. In fact, despite the expected amplification gain for the single-beam average intensity is much lower than the SRS threshold $g \ll g_{thres} \equiv 2\pi$, in an ensemble of ~ 2000 speckles, we expect that more than 60 of them have a local laser intensity overcoming it.

As shown in Fig.9, the experimental conditions are located in a region of the curve where the growth is significantly steep, far from the saturation. This explains the considerable enhancement observed for SRS in shots with the driver beams, although they provide an increase of density scalelength of only 10-20%.

It is also interesting to observe that the SRS reflectivity gets closer to the multispeckle model when the number of beams is progressively reduced (empty stars in Fig.9). This can be explained by recalling that the experimental gain is here calculated by considering the single-beam laser intensity. The above observation therefore suggests that collective processes result in a reduction of the SRS threshold with respect to single beam laser intensity, or - seen in a different way - an effective value of laser intensity given by the overlapped fields should be considered for computing the SRS gain, implying a larger number of speckles able to drive SRS. In this context, the speckle distribution given by the coherent overlapping of single-beam speckles should also be considered, suggesting a higher number of speckles and therefore also of high-intensity ones.

As suggested by the experimental results, the multi-beam irradiation produced a SRS light scattering in directions other than the backscattering. Analytical mod-

els suggest that multibeam SRS, where multiple laser beams couple to a common scattered e.m. wave, could occur at ICF conditions[21, 30]. However, while multi-beam TPD was extensively characterized in OMEGA experiments, multibeam SRS, which is expected to be dominant in long-scale NIF direct-drive experiments, still needs an accurate investigation. A first clear indication of sidescattered common-wave SRS was obtained by Depierreux et al.[41]; the results obtained in the present experiment provide a further evidence of the importance of collective SRS processes in determining the instability threshold and extent.

The conversion efficiency of hot electrons $\eta \sim 0.5\%$ agrees with the values obtained at OMEGA laser for small values of density scalelength[10] ($L \sim 100 - 150$ μm); moreover, the values of η and T_{hot} follow the correlation shown by Froula[9], suggesting that also in the present experiment HE are mainly accelerated by the damping of TPD EPWs. Stimulated Raman Scattering, also, show reflectivities one order of magnitude lower than the HE conversion efficiency, and can therefore only marginally contribute to their generation. A further confirmation of the origin of HE comes from the joint observation of optical and EMS data. When the driver beams are used, in fact, the $\omega_0/2$ spectra show that TPD slightly moves to regions of lower density, so that EPW wavevectors are expected to move to larger angles from the laser direction. This agrees with the slight increase of HE flux which was observed in the EMS looking the target at the larger angle (50°).

CONCLUSIONS

In the present experiment LPI is investigated by using a bundle of 9 partially-overlapped laser beams in an irradiation regime of interest for direct-drive inertial confinement fusion. Laser intensities are here intermediate between those envisaged for classical direct-drive scheme, massively explored at OMEGA laser facility and those expected in the Shock Ignition scheme. Experimental data show that TPD develops in a strongly saturated regime and turns off before the laser peak, while SRS steeply grows in linear convective regime in near-threshold conditions, therefore resulting in modest values of scattered light reflectivity. SRS reflectivity is well reproduced by considering the convective growth in independent speckles, where local laser intensities are distributed according to an exponential function and saturation of the SRS growth into the most intense speckles is taken into account. Despite the uncertainties about the distribution of local intensities into the speckles and about the noise level in the plasma, our basic model[23] satisfactorily reproduces the measured SRS reflectivity and confirms that SRS growth is in a regime far from saturation. Both SRS and TPD are shown to depend

on the overlapped laser intensity rather than on single beam intensity, suggesting that both the instabilities are collectively driven by multiple beams, therefore sharing common daughter waves. In case of SRS, this hypothesis is corroborated by the observation that light is predominantly scattered out of the lens cone.

Results also show that in the explored irradiation conditions, consisting in a transition region between the domain of TPD and SRS, the generation of HE is still dominated by TPD, giving rise to electrons with temperature around 20-50 keV and conversion efficiencies below 1% of laser energy.

ACKNOWLEDGEMENTS

This work has been carried out within the framework of the EUROfusion Consortium, funded by the European Union via the Euratom Research and Training Programme (Grant Agreement No 101052200 — EUROfusion). Views and opinions expressed are however those of the author(s) only and do not necessarily reflect those of the European Union or the European Commission. Neither the European Union nor the European Commission can be held responsible for them. The involved teams have operated within the framework of the Enabling Research Project: ENR-IFE.01.CEA “Advancing shock ignition for direct-drive inertial fusion”. This work was also done with the support and under the auspices of the NIFS Collaboration Research program (2021NIFS18KUGK123).

* gabriele.cristoforetti@cnr.it

- [1] J. Nuckolls, L. Wood, A. Thiessen, and G. Zimmerman, *Nature* **239**, 139 (1972).
- [2] R. S. Craxton, K. S. Anderson, T. R. Boehly, V. N. Goncharov, D. R. Harding, J. P. Knauer, R. L. McCrory, P. W. McKenty, D. D. Meyerhofer, J. F. Myatt, A. J. Schmitt, J. D. Sethian, R. W. Short, S. Skupsky, W. Theobald, W. L. Kruer, K. Tanaka, R. Betti, T. J. B. Collins, J. A. Delettrez, S. X. Hu, J. A. Marozas, A. V. Maximov, D. T. Michel, P. B. Radha, S. P. Regan, T. C. Sangster, W. Seka, A. A. Solodov, J. M. Soares, C. Stoeckl, and J. D. Zuegel, *Physics of Plasmas* **22**, 110501 (2015).
- [3] W. L. Kruer, in *Reading, M A, Addison-Wesley Publishing Co. (Frontiers in Physics. Volume 73), 1988, 199 p.*, Vol. 73 (1988).
- [4] C. S. Liu, M. N. Rosenbluth, and R. B. White, *Phys. Fluids* **17**, 1211 (1974).
- [5] W. L. Kruer, S. C. Wilk, B. B. Afeyan, and K. R. K, *Phys. Plasmas* **3**, 382 (1996).
- [6] J. Delettrez, T. Collins, and C. Ye, *Phys. Plasmas* **26**, 062705 (2019).
- [7] C. S. Liu and M. N. Rosenbluth, *Phys. Fluids* **19**, 967 (1976).
- [8] D. Froula, B. Yaakobi, S. Hu, P.-Y. Chang, R. Craxton, D. Edgell, R. Follett, D. Michel, J. Myatt, W. Seka, R. Short, A. Solodov, and C. Stoeckl, *Physical Review Letters* **108**, 165003 (2012).
- [9] D. Froula, D. Michel, I. Igumenshchev, S. Hu, B. Yaakobi, J. Myatt, D. Edgell, R. Follett, V. Yu, V. Glebov, V. Goncharov, T. Kessler, A. Maximov, P. Radha, T. Sangster, W. Seka, R. Short, A. Solodov, C. Sorce, and C. Stoeckl, *Plasma Phys. Control. Fusion* **54**, 124016 (2012).
- [10] C. Stoeckl, R. Bahr, B. Yaakobi, W. Seka, S. Regan, R. Craxton, J. Delettrez, R. Short, J. Myatt, and A. Maximov, *Physical Review Letters* **90**, 235002 (2003).
- [11] B. Yaakobi, P.-Y. Chang, A. Solodov, C. Stoeckl, D. Edgell, R. Craxton, S. Hu, J. Myatt, F. Marshall, W. Seka, and D. Froula, *Phys. Plasmas* **19**, 012704 (2012).
- [12] D. Michel, A. Maximov, R. Short, J. Delettrez, D. Edgell, S. Hu, I. Igumenshchev, J. Myatt, A. Solodov, C. Stoeckl, B. Yaakobi, and D. Froula, *Phys. Plasmas* **20**, 055703 (2013).
- [13] R. H. H. Scott, K. Glize, L. Antonelli, M. Khan, W. Theobald, M. Wei, R. Betti, C. Stoeckl, A. G. Seaton, T. D. Arber, D. Barlow, T. Goffrey, K. Bennett, W. Garbett, S. Atzeni, A. Casner, D. Batani, C. Li, and N. Woolsey, *Phys. Rev. Lett.* **127**, 065001 (2021).
- [14] M. Rosenberg, A. Solodov, J. Myatt, W. Seka, P. Michel, M. Hohenberger, R. Short, R. Epstein, S. Regan, E. Campbell, T. Chapman, C. Goyon, J. Ralph, M. Barrios, J. Moody, and J. Bates, *Phys. Rev. Lett.* **120**, 055001 (2018).
- [15] A. Solodov, M. Rosenberg, W. Seka, J. Myatt, M. Hohenberger, R. Epstein, C. Stoeckl, R. Short, S. Regan, P. Michel, T. Chapman, R. Follett, J. Palastro, D. Froula, P. Radha, J. Moody, and V. Goncharov, *Phys. Plasmas* **27**, 052706 (2020).
- [16] A. A. Solodov, M. J. Rosenberg, M. Stoeckl, A. R. Christopherson, R. Betti, P. B. Radha, C. Stoeckl, M. Hohenberger, B. Bachmann, R. Epstein, R. K. Follett, W. Seka, J. F. Myatt, P. Michel, S. P. Regan, J. P. Palastro, D. H. Froula, E. M. Campbell, and V. N. Goncharov, *Phys. Rev. E* **106**, 055204 (2022).
- [17] T. Tamagawa, Y. Hironaka, K. Kawasaki, D. Tanaka, T. Idesaka, N. Ozaki, R. Kodama, R. Takizawa, S. Fujioka, A. Yogo, D. Batani, P. Nicolai, G. Cristoforetti, P. Koester, L. Gizzi, and K. Shigemori, *Rev. Sci. Instrum.* **93**, 063505 (2022).
- [18] A. Curcio, P. Andreoli, M. Cipriani, G. Claps, F. Consoli, G. Cristofari, R. D. Angelis, D. Giulietti, F. Ingenito, and D. Pacella, *Journal of Instrumentation* **11**, C05011 (2016).
- [19] S. Agostinelli, J. Allison, K. Amako, J. Apostolakis, H. Araujo, P. Arce, M. Asai, D. Axen, S. Banerjee, G. Barrand, F. Behner, L. Bellagamba, J. Boudreau, L. Brogna, A. Brunengo, H. Burkhardt, S. Chauvie, J. Chuma, R. Chytrcek, G. Cooperman, G. Cosmo, P. Degtyarenko, A. Dell’Acqua, G. Depaola, D. Dietrich, R. Enami, A. Feliciello, C. Ferguson, H. Fesefeldt, G. Folger, F. Foppiano, A. Forti, S. Garelli, S. Giani, R. Giannitrapani, D. Gibin, J. Gómez Cadenas, I. González, G. Gracia Abril, G. Greeniaus, W. Greiner, V. Grichine, A. Grossheim, S. Guatelli, P. Gumplinger, R. Hamatsu, K. Hashimoto, H. Hasui, A. Heikkinen, A. Howard, V. Ivanchenko, A. Johnson, F. Jones,

- J. Kallenbach, N. Kanaya, M. Kawabata, Y. Kawabata, M. Kawaguti, S. Kelner, P. Kent, A. Kimura, T. Kodama, R. Kokoulin, M. Kossov, H. Kurashige, E. Lamanna, T. Lampén, V. Lara, V. Lefebure, F. Lei, M. Liendl, W. Lockman, F. Longo, S. Magni, M. Maire, E. Medernach, K. Minamimoto, P. Mora de Freitas, Y. Morita, K. Murakami, M. Nagamatu, R. Nartallo, P. Nieminen, T. Nishimura, K. Ohtsubo, M. Okamura, S. O'Neale, Y. Oohata, K. Paech, J. Perl, A. Pfeiffer, M. Pia, F. Ranjard, A. Rybin, S. Sadilov, E. Di Salvo, G. Santin, T. Sasaki, N. Savvas, Y. Sawada, S. Scherer, S. Sei, V. Sirotenko, D. Smith, N. Starkov, H. Stoecker, J. Sulkimo, M. Takahata, S. Tanaka, E. Tcherniaev, E. Safai Tehrani, M. Tropeano, P. Truscott, H. Uno, L. Urban, P. Urban, M. Verderi, A. Walkden, W. Wander, H. Weber, J. Wellisch, T. Wenaus, D. Williams, D. Wright, T. Yamada, H. Yoshida, and D. Zschesche, Nuclear Instruments and Methods in Physics Research Section A: Accelerators, Spectrometers, Detectors and Associated Equipment **506**, 250 (2003).
- [20] S. Atzeni, A. Schiavi, F. Califano, F. Cattani, F. Cornolti, D. Del Sarto, T. Liseykina, A. Macchi, and F. Pegoraro, Comput. Phys. Commun. **169**, 153 (2005).
- [21] D. DuBois, B. Bezzerides, and H. Rose, Phys. Fluids B **4**, 241 (1992).
- [22] H. A. Rose and D. F. DuBois, Phys. Fluids B **5**, 590 (1993).
- [23] G. Cristoforetti, S. Hüller, P. Koester, L. Antonelli, S. Atzeni, F. Baffigi, D. Batani, C. Baird, N. Booth, M. Galimberti, and et al., High Power Laser Science and Engineering **9**, e60 (2021).
- [24] W. Seka, B. B. Afeyan, R. Boni, L. M. Goldman, R. W. Short, K. Tanaka, and T. W. Johnston, Physics of Fluids **28**, 2570 (1985).
- [25] G. Cristoforetti, L. Antonelli, S. Atzeni, F. Baffigi, F. Barbato, D. Batani, G. Boutoux, A. Colaitis, J. Dostal, R. Dudzak, *et al.*, Physics of Plasmas **25**, 012702 (2018).
- [26] B. B. Afeyan and E. A. Williams, Phys. Rev. Lett. **75**, 4218 (1995).
- [27] R. L. Berger and L. V. Powers, The Physics of Fluids **28**, 2895 (1985).
- [28] W. Seka, D. H. Edgell, J. F. Myatt, A. V. Maximov, R. W. Short, V. N. Goncharov, and H. A. Baldis, Physics of Plasmas **16**, 052701 (2009).
- [29] G. Cristoforetti, L. Antonelli, D. Mancelli, S. Atzeni, F. Baffigi, F. Barbato, D. Batani, G. Boutoux, F. D'Amato, J. Dostal, R. Dudzak, E. Filippov, Y. J. Gu, L. Juha, O. Klimo, M. Krus, S. Malko, A. S. Martynenko, P. Nicolai, V. Ospina, S. Pikuz, O. Renner, J. Santos, V. T. Tikhonchuk, J. Trela, S. Viciani, L. Volpe, S. Weber, and L. A. Gizzi, High Power Laser Science and Engineering **7**, e51 (2019).
- [30] P. Michel, L. Divol, E. Dewald, J. Milovich, M. Hohenberger, O. Jones, L. Berzak Hopkins, R. Berger, W. Kruer, and J. Moody, Phys. Rev. Lett. **115**, 055003 (2015).
- [31] A. Tentori, A. Colaitis, W. Theobald, A. Casner, D. Raffestin, A. Ruocco, J. Trela, E. Le Bel, K. Anderson, M. Wei, B. Henderson, J. Peebles, R. Scott, S. Baton, S. Pikuz, R. Betti, M. Khan, N. Woolsey, S. Zhang, and D. Batani, Phys. Plasmas **28**, 103302 (2021).
- [32] A. Tentori, A. Colaitis, and B. D. Matter Radiat. Extremes **7**, 065902 (2022).
- [33] A. Tentori, A. Colaitis, and B. D. Matter Radiat. Extremes **7**, 065903 (2022).
- [34] R. Yan, A. Maximov, and R. Ren, Phys. Plasmas **17**, 052701 (2010).
- [35] A. Simon, R. Short, E. Williams, and T. Dewandre, Phys. Fluids **26**, 3107 (1983).
- [36] R. Yan, A. Maximov, C. Ren, and F. Tsung, Phys. Rev. Lett. **103**, 175002 (2009).
- [37] J. Meyer and H. Houtman, Phys. Fluids **28**, 1549 (1985).
- [38] M. N. Rosenbluth, Phys. Rev. Lett. **29**, 565 (1972).
- [39] R. Berger, E. Williams, and A. Simon, Physics of Fluids B: Plasma Physics **1**, 414 (1989).
- [40] G. Cristoforetti, A. Colaitis, A. Antonelli, S. Atzeni, F. Baffigi, D. Batani, F. Barbato, G. Boutoux, R. Dudzak, P. Koester, E. Krousky, L. Labate, P. Nicolai, O. Renner, M. Skoric, V. Tikhonchuk, and L. Gizzi, Europhys. Lett. **117**, 35001 (2017).
- [41] S. Depierreux, C. Neuville, C. Baccou, V. Tassin, M. Casanova, P.-E. Masson-Laborde, N. Borisenko, A. Orekhov, A. Colaitis, A. Debayle, G. Duchateau, A. Heron, S. Huller, P. Loiseau, P. Nicolai, D. Pesme, C. Riconda, G. Tran, R. Bahr, J. Katz, C. Stoeckl, W. Seka, V. Tikhonchuk, and C. Labaune, Phys. Rev. Lett. **117**, 235002 (2016).